



ASME Journal of Micro- and Nano-Manufacturing Online journal at:

https://asmedigitalcollection.asme.org/micronanomanufacturing



Sanjana Subramaniam

Department of Mechanical Engineering, Northwestern University, 2145 Sheridan Road B110, Evanston, IL 60208 e-mail: ssubramaniam@u.northwestern.edu

Jian Cao

Fellow ASME
Department of Mechanical Engineering,
Northwestern University,
2145 Sheridan Road A214,
Evanston, IL 60208
e-mail: jcao@northwestern.edu

Kornel Ehmann¹

Fellow ASME
Department of Mechanical Engineering,
Northwestern University,
2145 Sheridan Road L288,
Evanston, IL 60208
e-mail: k-ehmann@northwestern.edu

Multiphysics Analysis and Verification of Jet Flight in Electrohydrodynamic Printing for Near-Field Electrospinning Applications

Electrohydrodynamic (EHD) printing is a versatile process that can be used to pattern highresolution droplets and fibers through the deposition of an electrified jet. This highly complex process utilizes a coupled hydrodynamic and electrostatic mechanism to drive the fluid flow. While it has many biomedical, electronic, and filtration applications, its widescale usage is hampered by a lack of detailed understanding of the jetting physics that enables this process. In this paper, a numerical model is developed and validated to explore the design space of the EHD jetting process, from Taylor cone formation to jet impingement onto the substrate, and analyze the key geometrical and process parameters that yield highresolution structures. This numerical model applies to various process parameters, material properties, and environmental factors and can accurately capture jet evolution, radius, and flight time. It can be used to better inform design decisions when using EHD processes with distinct resolution requirements. [DOI: 10.1115/1.4065874]

1 Introduction

Electrohydrodynamic (EHD) printing is an additive manufacturing technique that yields high-resolution micro-/nanostructures [1]. Near-field electrospinning (NFES) takes advantage of this technique while using low voltages and small electrode separation distances to improve the precision and controllability of the charged fluid jet's deposition. It is a highly tunable process that is sensitive to ink material properties, environmental factors, and process parameters [2]. However, for a given material, the small electrode spacing restricts the process design space, which dictates the magnitude of the electric field that can be applied. This can lead to an incompatible time scale for excess solvent evaporation and charge dissipation, thus limiting the resolution and scalability of the printed structures. Therefore, it is paramount to collectively control the process variables, geometric parameters, and material properties to ensure that the final print meets the desired feature size for the targeted application. While experimental characterization is the most streamlined way to achieve real-time information on printed fiber morphology, it is also time-consuming in the parameter sweeps of all possible combinations of material, process, and environmental parameters. Numerical modeling serves as a viable alternative to speed up the application process and analyze the fundamental

multiphysics phenomena that underlie the electrohydrodynamic phenomenon.

Several relevant phenomena are important in the consideration of a physical process model [3–15]. The viscosity and surface tension forces work in tandem to attenuate the flow of the liquid ink that was destabilized by the presence of an electric field. The electric field, flow rate from a syringe pump, and gravity work to write the fluid onto the grounded substrate directly. Once the electrostatic force overcomes the surface tension force, a Taylor cone forms at the tip of the nozzle and a liquid jet develops to decrease the total surface area that experiences the destabilization, propelled by these parameters [3]. Moreover, the jetting fluid experiences destabilization due to surface tension and electrostatic forces, which can contribute to different EHD atomization modes, such as the dripping mode (dripping, microdripping, and spindle) and the jet mode (cone-jet, multijet, precession jet, and oscillating jet) [4]. Jet control is crucial to understanding the evolution of EHD printing and the final printed structure [5].

Many studies look at the theoretical and numerical modeling of far-field electrospinning jets, which use higher voltages and collector distances to print randomly oriented fibers [6]. While the core assumptions and the physics are similar, such as the leaky dielectric model [7], their results are not readily applicable to their near-field counterpart as the electric field distribution (i.e., the driving force of both processes) is not comparable. In terms of NFES, several theoretical models describe the jet evolution during the process [8,9]. Numerical models of near-field EHD processes (electrode spacing distances < 5 mm) using the volume of fluid [10–12], phase field [13], or level-set method (LSM) [14,15] have

World Congress on Micro and Nano Manufacturing (WVMNM-2023).
¹Corresponding author

Contributed by the Manufacturing Engineering Division of ASME for publication in the JOURNAL OF MICRO- AND NANO-MANUFACTURING. Manuscript received December 31, 2023; final manuscript received June 21, 2024; published online July 30, 2024. Assoc. Editors Brup Agreed.

been used to understand the jetting and deposition process as well as key material and process parameters that affect the numerical model. However, there is a large disconnect in directly applying this numerical study to improving the near-field EHD process itself. Most studies focus on qualitatively mimicking the process under a very tight distribution of process (low electrode spacing distances, fixed voltages) and geometrical (nozzle sizes smaller than those commercially available for continuous dispensing) parameters. In the literature, there is minimal quantification to how numerical simulations compare to experimental studies in jet deformation or deposition characteristics. Moreover, numerical simulation tools have not been used to explore the design space of the NFES process to improve its resolution. This knowledge gap is significant, as these parameters play a key role in the printed structure's overall deformation and it is difficult to analyze this aspect empirically, as it happens on the micron-scale.

To address the above-identified gap, a modular, flexible numerical model was developed and validated to effectively model an NFES jet under a variety of process and geometric parameters. This research contribution will allow for a streamlined determination of the ideal, optimal process conditions for a given electrospinnable solution to obtain a high-resolution EHD jet. In this work, a novel numerical formulation was proposed to interrupt the surface tension of the droplet during the initiation stage of electrospinning, akin to placing a glass rod near the syringe during the initiation process. This concept has been demonstrated experimentally in previous literature to initiate electrospinning jets without outside intervention [16]. Incorporating this modification into a numerical simulation enables a reduction in computational resources and allows for better modeling capabilities of the wide range of process parameters possible within the NFES design space without causing numerical instabilities. The model's generality accommodates arbitrary process parameters and material properties. Its versatility can be utilized to inform independently varying printing parameters for an arbitrary electrospinnable fluid ink and obtain its optimal process conditions. Moreover, the results presented in this paper provide a quantifiable way to validate the empirical trends that have been observed in the NFES of polymers. The applications of this work will widen the rapid adoption of NFES in which resolution and manufacturing time requirements are stringent, such as in the biomedical and electronic engineering space.

The paper is organized as follows: The governing equations and model formulation are presented in Sec. 2. Section 3 details the simulation methodology employed followed by the numerical simulation implemented with COMSOL MULTIPHYSICS, and the impact of each process parameter on the jet's deformation was quantified. In Sec. 4, experiments are presented to validate the numerical simulation results. Section 5 explores the conclusions and future directions of this work.

2 Governing Equations and Model Formulation

COMSOL MULTIPHYSICS 5.6 was used to model the EHD jet following the physics described in this section. An axisymmetric formulation was used to model the NFES jet, along the nozzle's axis, as seen in Fig. 1(a). The side profile of the nozzle is shown, with a 0.5 mm length, an inner radius (IR), and outer radius (OR). In this study, IR and OR reflect the dimensions used in experiments, i.e., 32-gauge $(54.0 \,\mu\text{m} \, \text{IR}, \, 117.5 \,\mu\text{m} \, \text{OR})$ and 34-gauge $(25.5 \,\mu\text{m} \, \text{IR}, \, 79.5 \,\mu\text{m})$ OR). The fluid and air domains are labeled as the black and the transparent regions, respectively. The separation distance between the nozzle (positive electrode) and the grounded substrate is represented by l_{sep} . The boundary conditions are summarized in Table 1. A high-voltage signal is applied to the nozzle walls, while a prescribed pressure is implemented at the nozzle opening. The substrate is grounded, and there is no pressure and velocity at the air and substrate boundaries. Finally, there is no charge density on the air domain's walls.

The axisymmetric assumption adequately describes the full NFES process with a cone-jet mode [12] while reducing

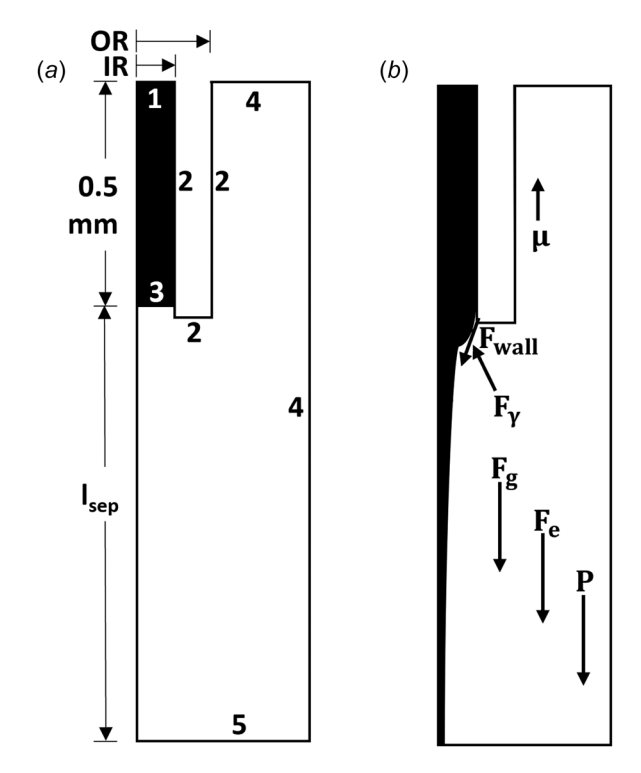


Fig. 1 Axisymmetric model formulation about nozzle axis: (a) simulation boundary conditions (black domain—ink, transparent domain—air), where boundaries 1–5 represent the nozzle inlet, nozzle wall, initial air–fluid interface, air domain wall, and substrate, respectively, and (b) force body diagram of EHD jet

computational time. This formulation can capture several configurations, such as dripping, pulsating, and cone-jet modes, but cannot model the tilted jet and twin jet modes. This simplification is an appropriate approximation if low enough voltages are used such that these nonaxisymmetric modes will not be induced [17]. The fluid ink used in this formulation was modeled as a Newtonian, leaky dielectric fluid [10]. It was assumed that the input material properties of the bulk material are representative of the material properties when nanoliters to microliters of the fluid are used in the electrospinning process.

The force body diagram of the jet is shown in Fig. 1(b). The governing equations underlying this multiphysics problem are summarized here. More detailed information on each formulation can be found elsewhere [15]. While the COMSOL MULTIPHYSICS software has been used to simulate EHD phenomena, this work is the first of its kind to use the formulation to explore the large NFES design space, quantify the impact of independently controlled process parameters to predict jet deformation, and assess the highest achievable resolution for a given electrospinning solution.

The laminar flow module was used to describe the fluid flow in the deforming jet, as the influence of a strong electric field employed in NFES induces a smooth, directed EHD flow from the electrified

Table 1 Boundary conditions in Fig. 1(a)

Boundary	Label	Boundary condition
Nozzle inlet Nozzle wall	1 2	$p = \rho g L + p_{\text{in}}$ $V = V_0$
Initial air-fluid interface	3	$F_e = \rho_e \mathbf{E} - \frac{1}{2} \mathbf{E}^2 \nabla \varepsilon$
Air domain wall	4	$p = 0$ $\mathbf{u} = 0$
Substrate	5	$\nabla \rho_e \cdot \mathbf{n} = 0$

nozzle to the grounded substrate. This module uses the mass conservation for incompressible flow (Eq. (1)) and the incompressible form of the Navier–Stokes equation (Eq. (2)), which are typically employed when solving hydrodynamic problems [15]. In these equations, ${\bf u}$ is the fluid velocity, ρ is the fluid density, p is the pressure, and μ is the fluid viscosity, i.e.,

$$\nabla \cdot \mathbf{u} = 0 \tag{1}$$

$$\frac{\delta \mathbf{u}}{\delta t} + \rho(\mathbf{u} \cdot \nabla)\mathbf{u} = -\nabla p + \nabla \cdot \mu[(\nabla \mathbf{u} + \nabla \mathbf{u}^{\mathrm{T}})]
+ (F_g + F_{\gamma} + F_{\text{wall}} + F_e)$$
(2)

The last term imposed in the Navier–Stokes equation is a sum of the external forces of gravity, $F_g = \rho g$, capillary force $F_{\rm wall}$, surface tension force F_{γ} , and electrostatic force F_e . The capillary and surface tension forces are given by

$$F_{\text{wall}} = \gamma \delta(\mathbf{n} \cdot \mathbf{n}_{\text{int}} - \cos \theta)(\mathbf{n}_{\text{int}} \cdot \mathbf{t}) - \frac{\mu}{\beta} \mathbf{u}_{\text{slip}}$$
(3)

$$F_{\gamma} = \gamma \delta \kappa \mathbf{n_{int}} + \delta \nabla_{s} \gamma \tag{4}$$

where γ represents surface tension, δ is the Dirac delta function, and κ is the fluid—air interface curvature. In the capillary force term, which is implemented on the nozzle inside wall tangent to the deforming fluid—air interface, \boldsymbol{n} is the unit normal to the interface, $\boldsymbol{n}_{\text{int}}$ represents the normal to the interface, θ is the contact angle between the fluid and nozzle wall, $(\mu/\beta)\boldsymbol{u}_{\text{slip}}$ is a frictional term, and θ is the slip length.

The electrostatics module was used to apply the electric field, as it can capture the electrodynamics of a leaky dielectric electrospinning ink under a strong electric field [10]. It implements the Gauss's law for volumetric charge density

$$\rho_e = \nabla \cdot (\varepsilon \mathbf{E}) \tag{5}$$

where ρ_e represents the charge density, the absolute permittivity is $\varepsilon = \varepsilon_0 \varepsilon_r$, ε_0 is the vacuum permittivity, ε_r is the relative permittivity, the electric field is $\mathbf{E} = -\nabla V$, and V is the electric potential. The electrostatic force was derived by taking the divergence of the Maxwell stress tensor \mathbf{T} [15]

$$F_e = \nabla \cdot \mathbf{T} = \rho_e \mathbf{E} - \frac{1}{2} \mathbf{E}^2 \nabla \varepsilon \tag{6}$$

This force was implemented as a volume force in the laminar flow module to couple the fluid's flow to the electric field applied in the electrostatics module, where the electric displacement field is represented by $\mathbf{D} = \varepsilon \mathbf{E}$.

The evolving air-fluid interface was tracked using the LSM

$$\frac{\delta\phi}{\delta t} + \mathbf{u} \cdot \nabla\phi = \lambda\nabla \cdot \left[\varepsilon_{\mathrm{LSM}}\nabla\phi - (1 - \phi)\frac{\nabla\phi}{|\nabla\phi|}\right]$$
 (7)
$$\Pi = \Pi_{\mathrm{air}} + \phi(\Pi_{\mathrm{ink}} - \Pi_{\mathrm{air}})$$

The level-set function (ϕ) was used to couple the LSM to other physics, such as electrostatics and laminar flow [13]. It can be used to calculate the effective material properties (Π) , given by

$$\Pi = \Pi_{\text{air}} + \phi(\Pi_{\text{ink}} - \Pi_{\text{air}}) \tag{8}$$

which can be substituted to determine the effective permittivity ($\varepsilon_{\rm eff}$), density ($\rho_{\rm eff}$), and dynamic viscosity ($\mu_{\rm eff}$) and where λ represents the LSM reinitialization parameter and $\varepsilon_{\rm LSM}$ is the transition thickness between the two phases.

3 Numerical Simulation Results

Section 3.1 reviews the implementation of the model formulation in Sec. 2 into the COMSOL MULTIPHYSICS software. Section 3.2 presents

the time sequence that a typical simulation follows, which is representative of all subsequent simulations detailed in Secs. 3.3–3.5. These sections focus on using this numerical simulation as a platform to better understand the impact of the process parameters, such as the nozzle size (32- and 34-gauge), voltage V_0 (1.5–3.0 kV), electrode separation distance $l_{\rm sep}$ (1–5 mm), and applied pressure P (0–13.8 kPa) on the jet's deformation, namely, the jet flight time and radius, both of which are explained in detail in Sec. 3.2.

3.1 Model Implementation. To complete the COMSOL MULTI-PHYSICS numerical simulation of the deforming EHD jet, a phase initialization step was used to configure the level-set method. Then, a time-dependent step was solved using the segregated MULTI-FRONTAL MASSIVELY SPARSE (MUMPS) direct solver with a backward Euler formulation. The coupled electrostatics, laminar flow, and level-set physics problem was solved, and jet evolution was tracked.

The ink solution incorporated into this simulation was a 600 kDa 1.0 wt % polyethylene oxide (Sigma Aldrich, Saint Louis, MO) dissolved in de-ionized water. The properties of both the ink and air domains are detailed in Table 2.

3.2 Sample Results. The time evolution of a sample EHD jet is shown in Fig. 3. The applied pressure (P) and voltage (V_0) for a 34-gauge nozzle were kept at 13.8 kPa and 2 kV, respectively, at an electrode separation distance $(I_{\rm sep})$ of 1.5 mm. At the beginning of the simulation, a prescribed pumping pressure and high-voltage DC signal are applied to the nozzle. A pendant drop forms at the tip of the nozzle to minimize the surface tension experienced by the fluid due to its hydrodynamic properties. Charges build up on the surface of the pendant drop, causing the surface to become increasingly electrostatically unstable. Eventually, the charge buildup generates

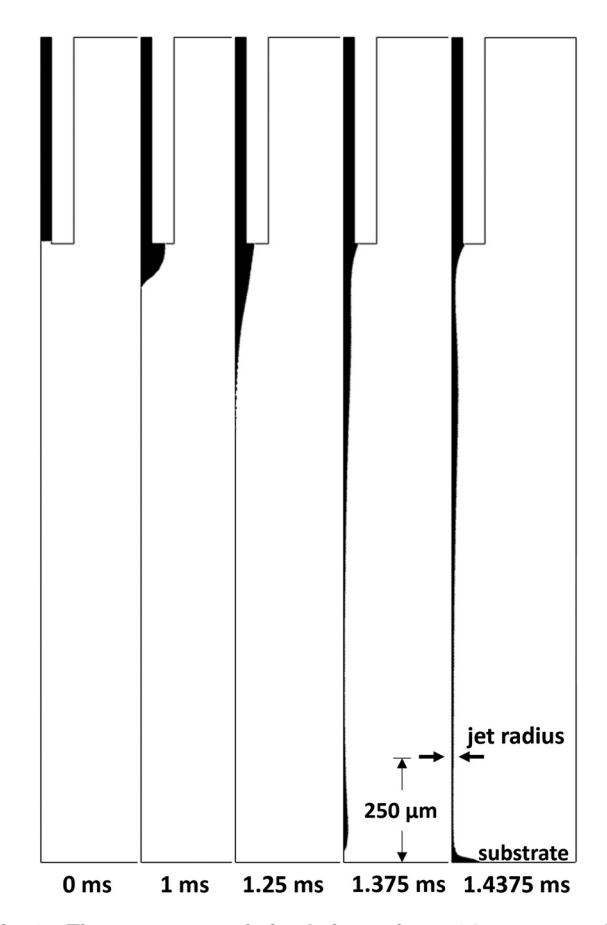


Fig. 2 Time sequence of simulation using a 34-gauge nozzle, $I_{\rm sep}=1.5$ mm, $V_0=2$ kV, and P=13.8 kPa. Jet radius is recorded at the time of impingement.

Table 2 Material properties used in the numerical simulation [13,18]

	Density ρ (kg/m ³)	Conductivity $K(\mu S/cm)$	Viscosity μ (mPa · s)	Surface tension γ (mN/m)	Dielectric constant ε
Air Ink	1.225 1.0	1×10^{-11} 62	$1.81 \times 10^{-2} \\ 20$	31.86	1 80

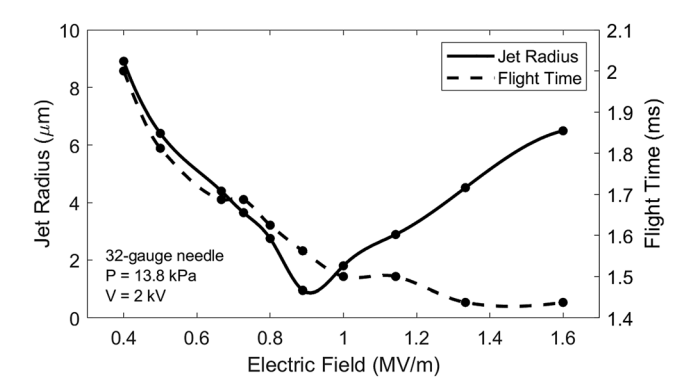


Fig. 3 Electric field influence on jet radius and flight time for a 32-gauge needle with an applied pressure of 13.8 kPa, and voltage of 2 kV

a downward electrostatic force that exceeds the surface tension force, and a Taylor cone forms at the tip of the nozzle, propelling the fluid jet toward the grounded substrate. The level-set method in the numerical formulation facilitates the fluid deformation during the entirety of the simulation. Typically, there is an increased radius of the droplet at the leading edge of the jet due to the accumulation of the pendant drop at the start of the process. The subsequent jet that follows is much thinner than the leading edge as it is not affected by the initial fluid buildup during the jet-initiation phase.

For this reason, the jet radius is recorded at $250 \, \mu m$ above the substrate at the time the jet reaches the substrate (i.e., the time of impingement or jet flight time). For this particular case, the jet radius is recorded as $2.27 \, \mu m$. This way of defining the jet radius translates well to the nonaxisymmetric nature of the ink deposition process, since the jet radius at this location is representative of the deposited fiber diameter when the substrate is moving. Sections 3.3-3.5 follow the methodology presented in this section while exploring the impact of different process parameters on the jet radius and flight time.

3.3 Electric Field Influence on Jet Radius and Flight Time. In this set of simulations, the applied pressure (P) and voltage (V_0) for a 32-gauge nozzle were maintained at 13.8 kPa and 2 kV, respectively. At the same time, the electrode separation distance $(l_{\rm sep})$ was varied from 1 mm to 5 mm (Fig. 4). Since the electric field strength is the ratio of the applied voltage to electrode separation distance $(l_{\rm sep})$, this set of simulations will yield a wide range of electric field values to elucidate the impact of this parameter on the printed jet. The jet radius, i.e., the radius of the jet 250 μ m above the substrate during the time of impingent, is recorded and compared as a function of the electric field.

Two different regimes are seen in Fig. 4. As the electric field rises from extremely low values (0.4–0.9 MV/m), there is a decrease in the jet radius and flight time. At lower electric fields, the fluid experiences a lower strain rate that contributes to its overall deformation, so its inertia prohibits it from reaching the smallest jet radius as it is energetically unfavorable. It correspondingly takes a longer time for the jet to reach the substrate. As the electric field increases, the comparably higher strain rate allows the jet to overcome the inertial force, so that the jet can stretch and thin according to its polymer relaxation kinetics. Overall, this phenomenon can be attributed to focusing on the jet from the increasing

electrostatic force, which accelerates the jet toward the substrate at a faster rate and yields more pronounced jet thinning. A minimum value of the jet radius is seen at 0.9 MV/m, after which the jet radius rapidly increases. At higher electric fields, the fluid jet accelerates toward the substrate at a timescale faster than the jet can thin, yielding a larger radius. This trend is witnessed in far-field electrospinning literature as well [19].

Several competing mechanisms at play help elucidate the parabolic behavior in jet radius seen in Fig. 4. Each polymer has a characteristic relaxation time, at which its molecules can stretch to their lowest energy configuration, given that this time is achievable during the process dynamics. For lower electric fields, inertial and viscous forces dominate, which inhibit the polymer from thinning within the short timescale of the jet's flight. A longer flight time would accommodate further jet thinning. Overall, the driving force—the electrically induced flow rate—is not strong enough to overcome the inertial and viscous forces, which are critical barriers for the polymer to stretch to its fullest extent. These phenomena contribute to a larger jet diameter at lower electric field values. At higher electric fields, the electrically induced flow rate supersedes any inertial and viscous forces at play, and a larger volume of polymer accelerates toward the substrate at a timescale much shorter than the critical time needed for the polymer to fully relax. Therefore, a larger diameter is seen at higher electric fields.

The minimization at $0.9\,\mathrm{MV/m}$ can attributed to the longer flight time that allows the jet to stretch more completely according to its polymer relaxation kinetics. It is shown that using these fixed material and process parameters, an electric field of $0.9\,\mathrm{MV/m}$ yields a high-resolution jet with a relatively short flight time.

3.4 Nozzle Radius Influence on Jet Radius and Flight Time. The nozzle size used for EHD printing forms the initial condition for the jet to print; any thinning that occurs will happen relative to the initial nozzle diameter, given that there is not a substantial charge accumulation of the fluid at the nozzle tip. Therefore, for continuous precision printing, it is advantageous to use the smallest possible nozzle diameter to adhere to the desired micro- and nanosized features; larger nozzles will result in larger sized features. For this analysis, equivalent flow conditions were used; the applied pressure (P) and voltage (V_0) were maintained at 13.8 kPa and 2 kV, respectively, for a 32-gauge (54.0 μm IR) and a 34-gauge nozzle (25.5 μ m IR). These nozzle sizes were chosen because they are the smallest commercially available sizes used for continuous jet printing. The radius curve for the 32- and 34-gauge nozzles follows the trend seen in Fig. 5. At lower electric fields, the jet radii when using a 34-gauge nozzle were slightly smaller than those using a 32-gauge nozzle, which can be attributed to the smaller initial condition and longer jet flight times that allows for adequate stretching. There is a minimum in the jet radius at 0.90 MV/m in both curves. However, the curves deviate significantly at electric fields > 0.90 MV/m. The 34-gauge nozzle yields much finer jet radii at higher electric fields, as the electrostatic force dominates in this regime, causing the decreased amount of fluid in the smaller 34-gauge nozzle to accelerate faster toward the substrate than that of the 32-gauge. Both experience insufficient stretching times and decreased flight times, but the 34-gauge nozzle jet is finer due to its initial nozzle radius, which is more influential on the final print when the voltage is substantially increased.

3.5 Comparison of Flow Rate and Electric Field Forces on Jet Deformation. While electrospinning is inherently an electrically driven process, there must be an adequate supply of fluid such

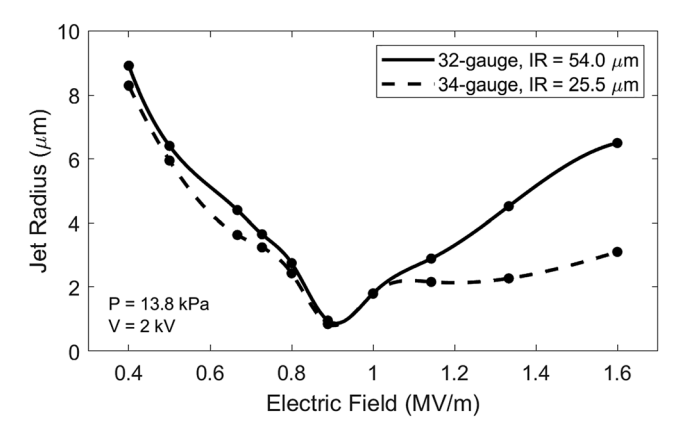


Fig. 4 Electric field influence on jet radius, comparison of the 32and 34-gauge needles with an applied pressure of 13.8 kPa, and voltage of 2 kV

that the rate of fluid depletion never exceeds the rate of supply. Ideally, the rate of supply would match the rate of printing. However, if high enough pressures are used to drive the fluid, the flow rate, rather than the electrostatic force, dictates the process, leading to larger jet diameters [13]. A balance must be achieved to make sure both the flow rate and electric field force constraints are compatible and maintained throughout the electrospinning process. While both factors influence the fluid's overall deformation, they do not have a proportional impact on its response. For this reason, it is unlikely that the trend seen in Figs. 4 and 5 will be repeated for this separate independent variable.

In this analysis, the applied voltage (V_0) for a 32-gauge nozzle was maintained at 2 kV, while the electrode separation distance (l_{sep}) and the pressure (P) were varied from 1 to 5 mm and 0 to 13.8 kPa (Fig. 6). For separation distances < 2 mm, no jet is observed as applying such a high electric field results in short circuit conditions. At pressures < 5.5 kPa, no jet is observed. In these cases, a pendant drop was present and became larger as the simulation progressed; an electrospinning jet did not form because the electrostatic forces were not able to overcome the surface tension forces holding the pendant drop intact. For applied pressures of 5.5 and 6.2 kPa, denoted in Fig. 6 by *, a pulsating jet was observed, in which the electrostatic forces would overcome the surface tension forces briefly to create a short-lived jet that accelerated toward the substrate. A larger diameter is seen here because the pendant drop accumulates enough fluid such that the electrostatic forces can briefly overcome the surface tension forces as the accumulated liquid is propelled toward the grounded substrate. However, the fluid supply rate is insufficient in sustaining a stable electrospinning jet over a longer timescale, so this cycle of accumulation and depletion will repeat. For

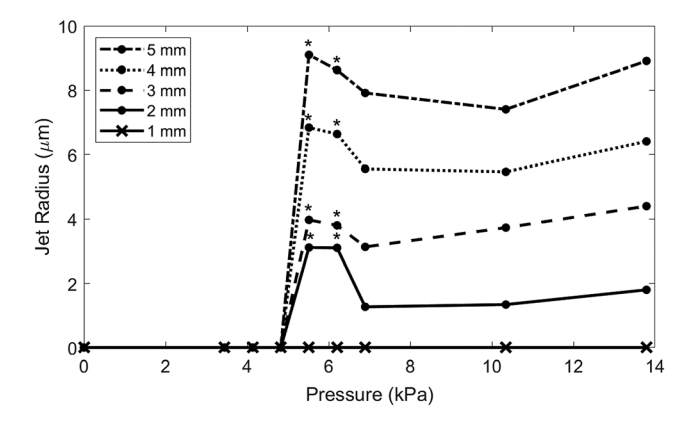


Fig. 5 Influence of pressure on jet radius for several electrode separation distances

pressures $> 6.2 \, \text{kPa}$, a stable electrospinning jet is formed and maintained to overcome the surface tension forces acting on the initial pendant drop. The jet radii are comparable at $6.9 \, \text{and} \, 10.3 \, \text{kPa}$, and a slight increase in the jet radius is observed when the applied pressure increases beyond $10.3 \, \text{kPa}$ due to increased fluid supply.

4 Experimental Verification of Numerical Simulation

To validate the proposed model in Sec. 2 and the numerical simulation results in Sec. 3, experiments were conducted on an electrospinning setup (Fig. 7) consisting of a three-axis stage (Aerotech ANT130XY and ATS100 Nanopositioning Stages), high-precision liquid dispensing system (Nordson EFD Ultimus V) with an attached 32 or 34-gauge stainless steel syringe (Hamilton Co.), humidity and temperature controlled chamber and monitoring (Vaisala HMP60 probe), conductive copper 110 substrate (McMaster Carr), and a high-voltage amplifier (Trek 10/10B-HS). The process was monitored using a CCD camera (Grasshopper GS3-U3-51S5M) with a telecentric lens (Edmund Optics) and a high-speed camera (FASTCAM Mini UX100 800K-M-16G) operating at 10,000 frames per second. All experiments were conducted at room temperature and 35% relative humidity.

The model ink solution used in the numerical simulation and experimental verification was an aqueous 600 kDa 1.0 wt % polyethylene oxide (material properties detailed in Table 2). Conductivity and viscosity measurements were obtained for the solution from previously published results [18]. The material properties of dynamic surface tension were characterized using pendant drop tensiometry. The dielectric constant was measured with an N1501A dielectric kit and a vector network analyzer (Keysight Technologies).

This validation focused on assessing the influence of the independently varying process parameters (pressure, voltage, separation distance, and nozzle size) on the jet radius and flight time. The flight time was defined as the time it took for the initiated jet to accelerate toward and impinge upon the substrate. The jet radius was measured at the time of impingement, $250 \, \mu \text{m}$ above the substrate, to avoid the distortion that occurs due to fluid accumulation on the substrate (Fig. 8). The experimentally determined jet radius and flight time values were qualitatively and quantitatively compared to the simulation results to assess the model's accuracy.

To validate the influence of applied pumping pressure on jet deformation in both simulations and experiments, the pressure (P) was varied from 6.9 to 13.8 kPa while keeping the separation distance (I_{sep}) and voltage (V_0) for a 32-gauge nozzle at 2 mm and

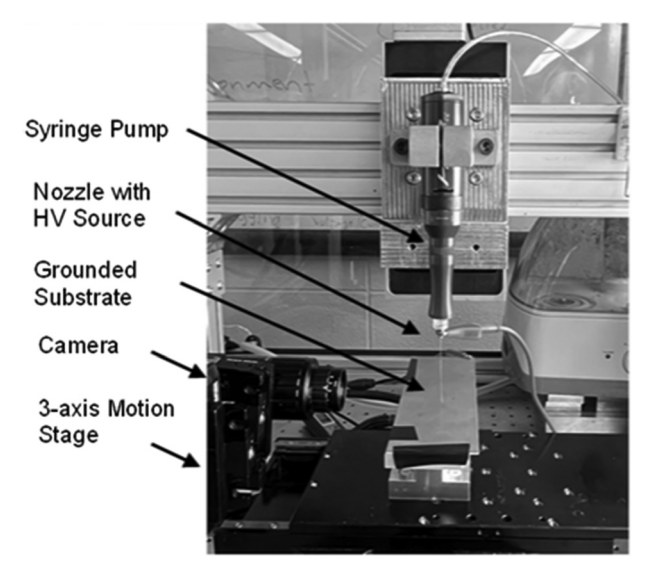


Fig. 6 Experimental setup



Fig. 7 Experimental model validation

Table 3 Experimental validation of applied pressure

P (kPa)	Flight time (ms)		Jet radius (μm)	
	Simulation	Experiment	Simulation	Experiment
6.9	2.2	2.4±0.1	1.30	3.65±0.10
10.3	2.1	2.1 ± 0.1	1.97	6.49 ± 0.40
13.8	2.0	2.1 ± 0.2	2.07	7.80 ± 0.55

1.5 kV (Table 3). While the experimental jet radii skew higher than those obtained by simulations, the flight times are comparable.

To compare the numerical simulation and experimental results of the applied voltage on the jet deformation, the voltage (V_0) was varied from 1.5 to 3.0 kV while keeping the separation distance $(l_{\rm sep})$ and applied pressure (P) for a 32-gauge nozzle at 2 mm and 13.8 kPa, respectively (Fig. 9). Experimental data points and corresponding error bars represent the average of five separate experimental trials. As in the previous comparison, the experimental flight times for all data points were within 0.2–0.4 ms of the simulation flight times, while the experimental jet radii demonstrate the same trend as the simulated radii but are considerably larger in magnitude than the simulated jet radii. Regarding the comparison of the simulations and experiments for the jet radius, the nozzle size, i.e., 32- and 34-gauge nozzles, and the separation distance $(l_{\rm sep})$ from 2 to 5 mm were varied while keeping the pressure (P) and voltage (V_0) at 13.8 kPa and 2 kV. Figure 9 depicts the comparison. The experimental results

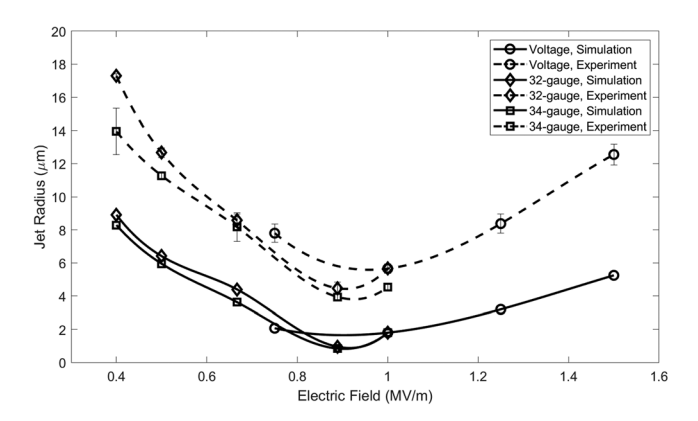


Fig. 8 Experimental validation of separation distance, voltage, and nozzle size

shown replicate those in Fig. 5. Experimental results for electric field values > 1 MV/m, i.e., separation distances < 2 mm, are not included in this analysis since for such values, short circuit conditions would occur.

In general, the numerical simulations qualitatively match the jet initiation and deformation. There is good agreement in the parabolic trend seen in the jet radius as a function of the electric field both in simulation and experiment. Quantitatively, the experimental values skew higher than the simulation results. The observed discrepancies in accuracy were attributed to the assumptions made in the simulations, i.e., the omission of the charge convection that promotes surface charge self-repulsion or the omission of extensional rheology which would generate a different deformation response than from the steady-state shear viscosity used in these simulations. The lack of precision in obtaining the experimental observations could be attributed to slight jet bending from the neutral axisymmetric position, which would distort the measured reading of the jet diameter within the depth of field of the camera.

5 Conclusion and Future Directions

In this study, a numerical model was developed and validated to describe the deformation and time evolution of an EHD jet. The ideal conditions to achieve a high-resolution jet were determined. The role of applied pressure, voltage, separation distance, and nozzle size were quantified numerically and experimentally verified in terms of jet radius and flight time. The generality of this model allows different electrospinnable fluid inks to be evaluated quickly to determine their optimal process conditions. Overall, it can aid and inform ink design based on the desired fiber diameter, which will save processing time. Future work will focus on quantifying the impact of material properties that are dependently related, conductivity variations, and evaporation on the jet radius and flight time. This implementation will estimate the accumulated charge on the printed structure, which has a significant impact, as electrostatic repulsion mitigates the formation of multilayer structures.

Acknowledgment

The authors would like to thank Dr. Aleia Bellcross, Dr. Emily Ma, Dr. Jana Butman, and Dr. Bhumi Bhusal for their help in obtaining material properties, and Dr. Nicolas Martinez-Prieto for his technical support and discussions.

Funding Data

 National Science Foundation (NSF) (Grant Nos. CMMI 1934350 and DMR-1720139; Funder ID: 10.13039/ 100000084).

Data Availability Statement

The authors attest that all data for this study are included in the paper.

Nomenclature

 $\mathbf{D} = \text{electric displacement field}$

 $\mathbf{E} = \text{electric field}$

 F_e = electrostatic force

 $F_{\text{wall}} = \text{capillary force}$

 F_{ν} = surface tension force

 \dot{K} = electrical conductivity

 $l_{\rm sep}=$ separation distance between the nozzle (positive electrode)

and the grounded substrate

n =unit normal to the interface

 $n_{\text{int}} = \text{normal to the interface}$

P = pressure

T = Maxwell stress tensor

 $\mathbf{u} = \text{velocity}$

- V = electric potential
- $\beta = \text{slip length}$
- $\gamma = \text{surface tension}$
- $\delta = \text{Dirac delta function}$
- ε = absolute permittivity, dielectric constant
- ε_{LSM} = transition thickness between the two phases
 - ε_r = relative permittivity
 - $\varepsilon_0 = \text{vacuum permittivity}$
 - $\theta = \text{contact}$ angle between the fluid and nozzle wall
 - κ = fluid–air interface curvature
 - $\lambda = LSM$ reinitialization parameter
 - $\mu = viscosity$
 - Π = effective material properties
 - $\rho = \text{density}$
 - $\rho_e = \text{charge density}$
 - ϕ = level-set function

References

- [1] Onses, M. S., Sutanto, E., Ferreira, P. M., Alleyne, A. G., and Rogers, J. A., 2015, "Mechanisms, Capabilities, and Applications of High-Resolution Electrohydro-
- dynamic Jet Printing," Small, 11(34), pp. 4237–4266.

 [2] Mkhize, N., and Bhaskaran, H., 2022, "Electrohydrodynamic Jet Printing: Introductory Concepts and Considerations," Small Sci., 2(2), p. 2100073.

 [3] Phung, T. H., Oh, S., and Kwon, K. S., 2018, "High-Resolution Patterning Using
- Two Modes of Electrohydrodynamic Jet: Drop on Demand and Near-Field Electrospinning," J. Visualized Exp., 2018(137), p. 57846.
 [4] Montanero, J. M., and Ganan-Calvo, A. M., 2019, "Dripping, Jetting and Tip
- Streaming," Rep. Prog. Phys., 83(9), p. 097001.
- [5] Robinson, T. M., Hutmacher, D. W., and Dalton, P. D., 2019, "The Next Frontier in Melt Electrospinning: Taming the Jet," Adv. Funct. Mater., 29(44), p. 1904664.
- [6] Lauricella, M., Succi, S., Zussman, E., Pisignano, D., and Yarin, A. L., 2020, 'Models of Polymer Solutions in Electrified Jets and Solution Blowing," Rev. Mod. Phys., 92(3), p. 035004.

- [7] Saville, D. A., 1997, "Electrohydrodynamics: The Taylor-Melcher Leaky Dielectric Model," Annu. Rev. Fluid Mech., 29(1), pp. 27-64.
- Ru, C., Chen, J., Shao, Z., Pang, M., and Luo, J., 2014, "A Novel Mathematical Model for Controllable Near-Field Electrospinning," AIP Adv., 4(1), p. 017108.
- [9] Chen, J., Shao, Z., Ru, C., and Yang, Z., 2013, "Mathematical Analysis for Controllable Near-Field Electrospinning," 2013 International Conference on Manipulation, Manufacturing and Measurement on the Nanoscale, Suzhou, China, Aug. 26-30, pp. 207-210.
- [10] Guan, Y., Wang, M., Wu, S., Tian, Y., Ye, D., and Huang, Y. A., 2023, "Modeling and Analysis of Electrohydrodynamic Printing Under Various Pulsed Voltage Waveforms," Microfluid. Nanofluid., 27(2), pp. 1–10.
- [11] Pan, Y., and Zeng, L., 2019, "Simulation and Validation of Droplet Generation Process for Revealing Three Design Constraints in Electrohydrodynamic Jet
- Printing," Micromachines (Basel), **10**(2), p. 94. [12] Lastow, O., and Balachandran, W., 2006, "Numerical Simulation of Electrohydrodynamic (EHD) Atomization," J. Electrostat., 64(12), pp. 850-859
- [13] Singh, S. K., and Subramanian, A., 2020, "Phase-Field Simulations of Electrohydrodynamic Jetting for Printing Nano-to-Microscopic Constructs," RSC Adv., 10(42), pp. 25022-25028.
- [14] Farjam, N., Spiegel, I. A., and Barton, K., 2022, "High-Fidelity Modeling and Validation of Electrohydrodynamic Jet Printing," Materialia (Oxf), 26, p. 101578.
- [15] Mohammadi, K., Movahhedy, M. R., and Khodaygan, S., 2019, "A Multiphysics Model for Analysis of Droplet Formation in Electrohydrodynamic 3D Printing Process," J. Aerosol Sci., 135, pp. 72-85.
- [16] He, L., 2017, "Control and Predictability of Near-Field Electrospinning," Ph.D. thesis, University of California, Irvine, CA.
- [17] Hartman, R. P. A., Brunner, D. J., Camelot, D. M. A., Marijnissen, J. C. M., and Scarlett, B., 2000, "Jet Break-Up in Electrohydrodynamic Atomization in the Cone-Jet Mode," J. Aerosol Sci., 31(1), pp. 65–95.
- [18] Martinez-Prieto, N., Fratta, G., Cao, J., and Ehmann, K. F., 2018, "Deposition of Variable Bead Diameter Arrays by Self-Focusing Electrohydrodynamic Jets," ASME J. Micro Nano-Manuf., 6(3), p. 031003.
- [19] Wu, C. M., Chiou, H. G., Lin, S. L., and Lin, J. M., 2012, "Effects of Electrostatic Polarity and the Types of Electrical Charging on Electrospinning Behavior," J. Appl. Polym. Sci., 126(Suppl. 2), pp. E89–E97.